

Gold Adparticles on Silver Combine Low Overpotential and High Selectivity in Electrochemical CO₂ Conversion

Adnan Ozden,^{II} Yanjiang Liu,^{II} Cao-Thang Dinh,^{II} Jun Li, Pengfei Ou, F. Pelayo García de Arquer, Edward H. Sargent,* and David Sinton*



Cite This: ACS Appl. Energy Mater. 2021, 4, 7504–7512



Read Online

ACCESS |

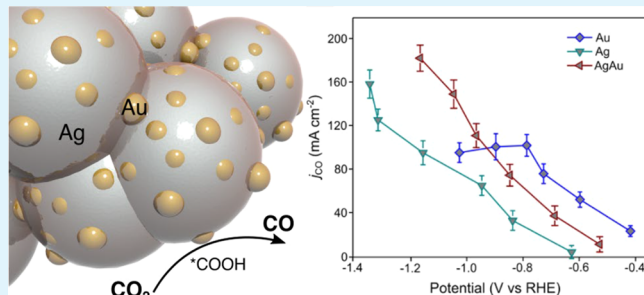
Metrics & More

Article Recommendations

Supporting Information

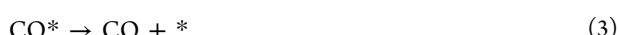
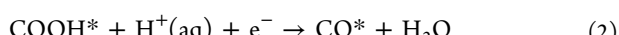
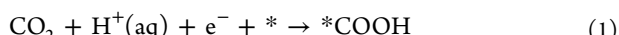
ABSTRACT: Silver (Ag) catalysts enable high selectivity (>90%) in CO₂-to-CO conversion at >100 mA cm⁻²; gold (Au) catalysts are active at lower overpotential, but with lower selectivity (<80%). Here we present an adparticle-functionalized catalyst that combines the benefits of each by uniting Au adparticles on the AgAu interface. Au adparticles modify the lattice and electronic structure of Ag and lower the free energy change required to form *COOH. We demonstrate selective and low-overpotential CO₂-to-CO conversion at >490 mA cm⁻² in a flow cell. In a membrane electrode assembly, the catalyst achieves 90% CO selectivity and 33% CO energy efficiency over 60 h.

KEYWORDS: CO₂ electroreduction, CO production, energy materials, catalyst design, membrane electrode assembly, energy efficiency, carbon efficiency, overpotential



Renewable electricity-powered electrochemical CO₂ reduction (CO₂RR) is a route to the net-zero-emission production of chemicals and fuels that are currently produced via energy- and carbon-intensive industrial processes.^{1–4} Carbon monoxide (CO) is a common industrial feedstock and the input for Fischer–Tropsch-based production of hydrocarbon.⁵ CO can also be further reduced to mult carbon products (e.g., ethylene, acetate, and *n*-propanol) via CO electroreduction process.^{6–10} The conversion of CO₂-to-CO requires fewer electrons and protons (2e⁻/2H⁺) and has been achieved with near-unity selectivities (>90%) at industrially relevant reaction rates (>100 mA cm⁻²).^{11,12}

Electrochemical CO₂-to-CO conversion starts with the formation of *COOH intermediate. Surface adsorbed *COOH is then reduced to *CO via electron transfer and desorbed, as shown in eqs 1–3.^{13,14} An ideal CO₂-to-CO catalyst would provide an adsorption strength that facilitates both *COOH formation and the *CO desorption steps.^{15,16}



Present-day low-temperature CO₂-to-CO conversion is performed on heterogeneous catalysts such as silver (Ag),^{17,18} gold (Au),^{19,20} and palladium (Pd).^{21,22} Ag and Au exhibit the highest selectivities to CO (>80%).²³ Ag can mediate CO₂-to-CO conversion at practical productivities > 100 mA cm⁻². However, this high activity comes at the

expense of high overpotentials. A practical level of activity (CO partial current density of >150 mA cm⁻²) at low applied potentials (<-1 V versus the reversible hydrogen electrode (RHE)) are required for the practicality of the CO₂-to-CO conversion process.^{24–26} Au achieves CO₂ conversion at lower overpotentials but suffers low selectivity (<90%) at production rates greater than 100 mA cm⁻²,²⁶ as the hydrogen evolution reaction (HER) takes over. These limitations prevent conventional Au and Ag catalysts from achieving high energy efficiency at industrially relevant reaction rates.²⁷

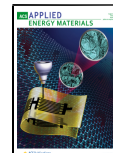
Here we report an activity-promoting strategy that combines the selectivity of Ag with the activity of Au, reduces the energy barrier for CO₂ activation, and thereby enables high energy efficiency CO₂-to-CO conversion. Using density functional theory (DFT) calculations, we find that undercoordinated Au atoms at the AgAu interface significantly decrease the formation energy of *COOH (CO₂ + H⁺ + e⁻ → *COOH), reducing the overpotential in CO₂-to-CO conversion.

We implement the Au-doping strategy on planar catalysts (sputtered Ag on porous polytetrafluoroethylene (PTFE) with Au-doping via galvanic replacement, 2D AgAu), and high-surface-area catalysts (Au-doped Ag nanoparticles on 2D AgAu

Received: June 2, 2021

Accepted: July 22, 2021

Published: July 26, 2021



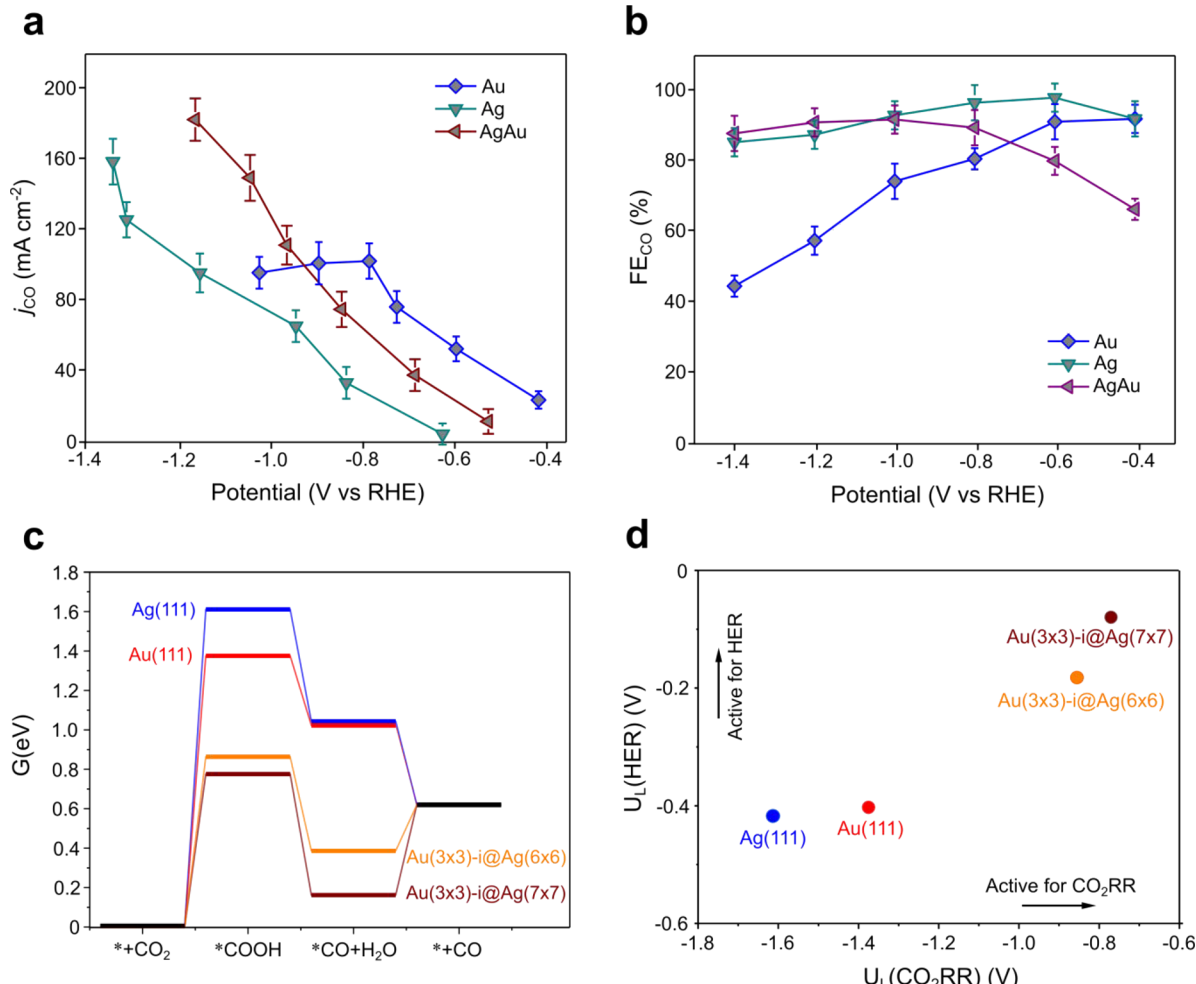


Figure 1. Mechanistic understanding. (a) CO partial current density versus potential. (b) CO FE versus potential. (c) Free energy diagram for CO₂RR to CO in all models. (d) Calculated limiting potential for HER versus that for CO₂RR. Right and upper regions denote high activity for CO₂RR and HER, respectively. Note: AgAu catalyst stands for Au-doped planar Ag/PTFE (with an optimized galvanic-replacement duration of 15 min), 2D Ag catalyst stands for planar (2D) Ag/PTFE, and 2D Au catalyst stands for planar (2D) Au/PTFE.

and 3D AgAu; see *Supporting Information* methods for details). In a gas diffusion electrode-based flow cell electrolyzer, 2D AgAu and 3D AgAu catalysts yield CO FEs exceeding 90% at CO partial current densities up to 165 and 350 mA cm^{-2} , respectively. These AgAu catalysts exhibit ~ 200 mV lower onset potentials compared to the undoped Ag controls. In a membrane electrode assembly (MEA) electrolyzer, the 3D AgAu catalysts enable CO FEs of >90% and CO full-cell EEs of >30% over a wide range of CO partial current densities from 105 mA cm^{-2} to 240 mA cm^{-2} . The MEA system equipped with a 3D AgAu catalyst enables stable CO electrosynthesis for 60 h at a current density of 200 mA cm^{-2} , with an average CO FE of 90% and average full-cell EE of 33%. At an average current density of 185 mA cm^{-2} , the system also maintains an average single pass CO₂ conversion of 33% for 60 h.

RESULTS AND DISCUSSION

We analyzed the origins of the limitations of conventional Ag and Au catalysts at practical reaction rates (>100 mA cm^{-2}): (1) high cathodic overpotential on Ag and (2) high HER activity on Au. Using planar Ag/PTFE and Au/PTFE catalysts, we investigated the CO₂RR performance in 1 M KHCO₃ over a voltage range of -0.41 and -1.36 V versus the RHE (see *Supporting Information* experimental procedures for details).

We found that CO partial current density increases with increasing applied potential on both Ag/PTFE and Au/PTFE catalysts (Figure 1a,b and see *Supporting Information* Tables S1 and S2 for additional experimental details). On Au/PTFE catalyst, the CO FE remains above 90% up to a current density of 60 mA cm^{-2} and a potential of -0.57 V versus RHE (Figure 1a,b and see Table S1 for additional experimental details). A further increase in the current density results in HER dominating CO₂RR, and the partial current density is capped at ~ 100 mA cm^{-2} at -0.71 V versus RHE (58% CO FE at 176 mA cm^{-2} and at -0.88 V versus RHE) (Figure 1a,b and see Table S1 for additional experimental details). On the Ag/PTFE catalyst, the CO selectivity remains above 90% up to a current density of 120 mA cm^{-2} , albeit with a cathodic overpotential of -1.32 V versus RHE (Figure 1a,b and see Table S2 for additional experimental details). The CO partial current density reaches its plateau of ~ 160 mA cm^{-2} at -1.36 V versus RHE (86% CO FE at 186 mA cm^{-2}) (Figure 1a,b).

To provide mechanistic insights into the electrochemical activity of Ag and Au toward CO₂-to-CO conversion, we carried out density functional theory (DFT) calculations of adsorption geometries and energetics (Figure 1c and see Figures S1–S3 for additional experimental details). The DFT calculations predict that the free energies to form *COOH

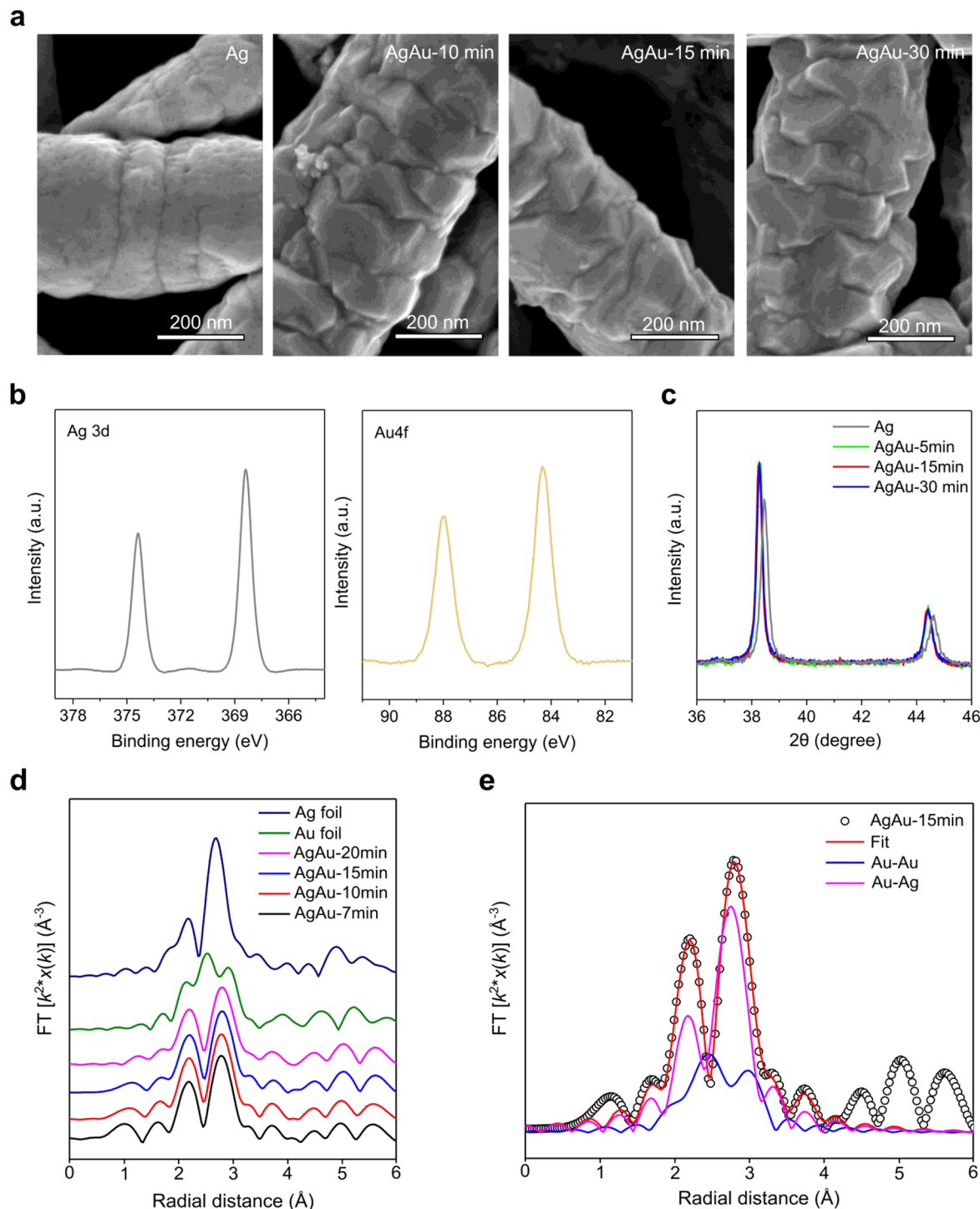


Figure 2. Characterization of planar (2D) AgAu catalysts. (a) SEM images of AgAu catalyst. The SEM images illustrate the growth of dendrites with extending duration of galvanic-replacement duration, whereby extending duration of galvanic-replacement results in structured deposits. Scale bars are 200 nm. (b) XPS spectra of AgAu catalyst. The Ag 3d and Au 4f signals indicate the coexistence of Ag and Au in the AgAu catalyst. (c) XRD spectra of the 2D AgAu catalyst. (d) Au L₃-edge EXAFS spectra of various AgAu catalysts in comparison with those of Ag and Au foils. (e) Au L₃-edge EXAFS fitting results for the AgAu-15 min catalyst. Red curves are cumulative fitting spectra. Blue and pink curves represent Au–Au and AgAu scattering paths, respectively. Note: AgAu catalyst stands for Au-doped planar Ag/PTFE (with an optimized galvanic-replacement duration of 15 min). AgAu-5 min, AgAu-7 min, AgAu-10 min, AgAu-15 min, AgAu-20 min, and AgAu-30 min stand for the catalysts with 5, 7, 10, 15, 20, and 30 min of galvanic-replacement durations.

(ΔG_{COOH})—potential-determining step in CO₂RR—on pure Ag and Au are 1.61 and 1.38 eV, respectively (Figure 1c). Tafel analyses of CO productivities from CO₂ on pure Ag and Au give slopes of 137 and 44 mV dec⁻¹, suggesting that CO₂ + H⁺ + e⁻ → *COOH is the rate-limiting step for CO₂ reduction to

CO (see Figure S4 for Tafel slopes). We then sought to find the possible materials structure combinations that would lower the free energy to form *COOH and found that the island models (“i”) (i.e., islands of gold particles on Ag—Figures S1 and S2) lower the free energy required to form *COOH, such

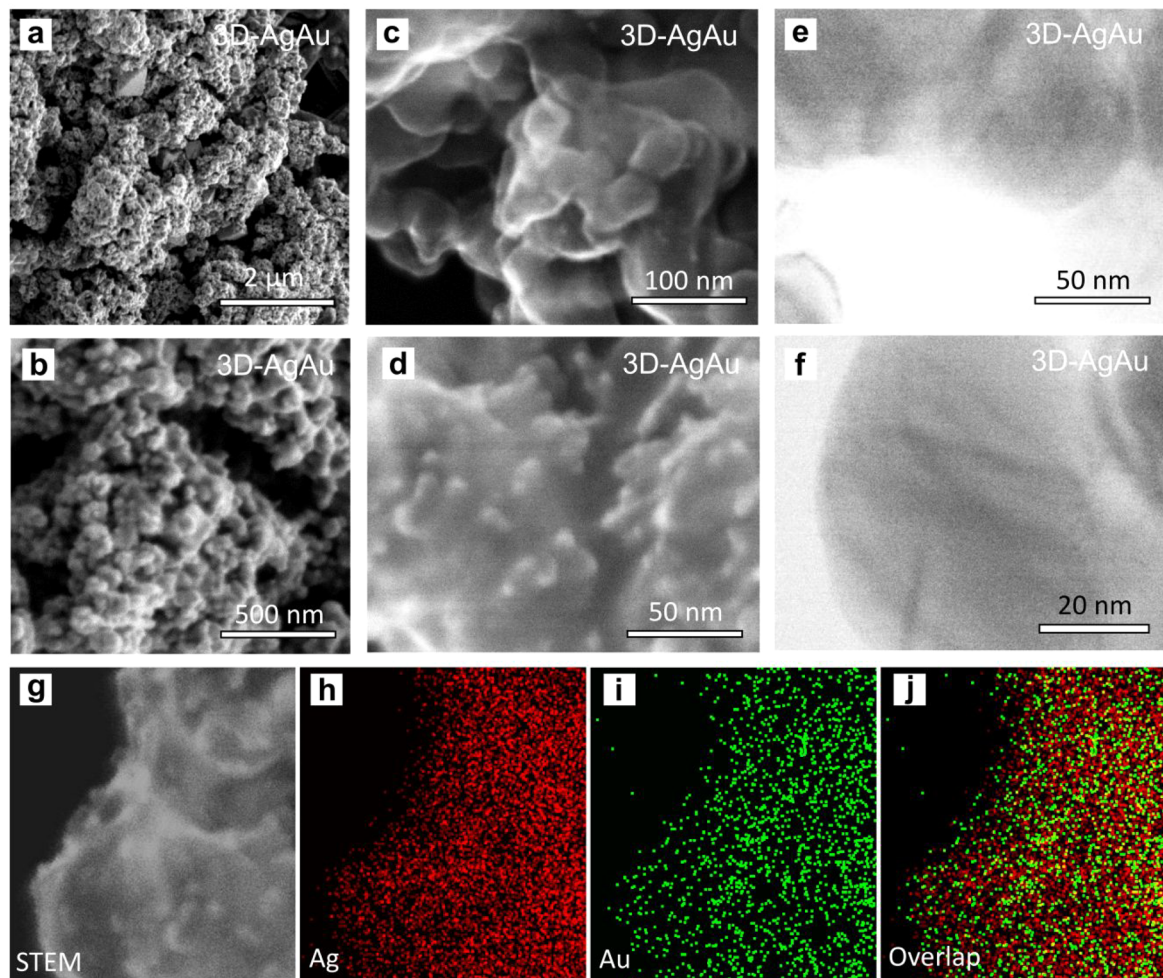


Figure 3. Characterization of 3D AgAu catalysts. (a, b) SEM images of the Au-doped Ag NPs formed on the 2D Ag/PTFE substrates. Scale bars are $2\ \mu\text{m}$ and $500\ \text{nm}$, respectively. (c, d) TEM images of the Au-doped Ag NPs. 15 min of galvanic replacement between the Ag and Au atoms leads to growth of small islands on the surface of the Ag NPs. Scale bars are 100 and $50\ \text{nm}$, respectively. (e, f) TEM images of the Au-doped Ag NPs. Scale bars are 50 and $20\ \text{nm}$, respectively. (g) HAADF-STEM image of the 3D AgAu catalysts. (h) EDX elemental mapping of Ag. (i) EDX elemental mapping of Au. (j) EDX elemental mapping of Au and Ag. Scale bars of HAADF-STEM images and EDX mappings are $50\ \text{nm}$. Note: 3D AgAu catalyst stands for Au-doped Ag NPs supported on planar 2D AgAu catalyst (each with the galvanic-replacement duration of 15 min).

that both $\text{Au}(3 \times 3)\text{-i@Ag}(6 \times 6)$ ($0.86\ \text{eV}$) and $\text{Au}(3 \times 3)\text{-i@Ag}(7 \times 7)$ ($0.78\ \text{eV}$) possess smaller ΔG^*_{COOH} than $\text{Ag}(1.61\ \text{eV})$ and $\text{Au}(1.38\ \text{eV})$ (Figure 1c,d). The presence of undercoordinated Au in the island case led to preferential binding of ${}^*\text{C}$ species. Ag also has a higher affinity for ${}^*\text{O}^{28}$ and thus further stabilizes ${}^*\text{COOH}$. The configuration of ${}^*\text{COOH}$ here provides bifunctional²⁹ binding sites for C–Au and O–Ag—a feature of the AgAu combination not present in pure Ag or Au cases due to the unstable Ag bound with ${}^*\text{C}$ and the fully coordinated nature of Au. For island cases, the enhancement in $U_L(\text{CO}_2\text{RR})$ outweighs $U_L(\text{HER})$ (Figure 1d), due to the undercoordinated Au species. These findings suggest the opportunity to achieve, via AgAu catalysts, the combination of high CO productivity and low overpotential.

Encouraged by the DFT findings, we took the view that by decreasing the CO_2 activation barrier and suppressing HER on Ag—via Au islands—we could lower the overpotential toward CO_2 -to-CO conversion and thereby attain high EE.

To test this hypothesis, we prepared a set of 2D AgAu catalysts with different morphologies using a galvanic-replacement reaction. The galvanic replacement was performed by immersing Ag/PTFE catalysts in a homogeneous mixture of

deionized (DI) water and acetone containing $1\ \text{mM}\ \text{AuCl}_3$ for various durations, from 5 to 30 min (see Supporting Information methods for details). Scanning electron microscopy (SEM) images show the growth of adparticles on the surface of Ag/PTFE fibers as a function of galvanic-replacement duration (Figure 2a and see Figure S5 for additional SEM images). Low-magnification SEM images indicate that the galvanic-replacement process does not alter the microscale pore structure of the AgAu/PTFE (see Figure S6 for low-magnification SEM images). X-ray photoelectron spectroscopy (XPS) peaks corresponding to Ag 3d and Au 4f confirm the coexistence of Au and Ag on the surface of the resulting electrode (Figure 2b). We compared the XPS spectra of 2D AgAu catalysts with those of pure Au and Ag foils. We observed positive peak shifts of the 2D AgAu catalysts in both Au and Ag plots, indicating electron withdraws from Au 4f and Ag 3d orbitals. This charge transfer between Au and Ag clearly shows an electronic modification of Ag catalysts with the addition of Au adparticles (see Figure S7 for XPS peaks). X-ray diffraction (XRD) studies of the 2D AgAu and 2D Ag control catalysts show that Au-doping results in a negative shift in the crystal phase of Ag, indicating a lattice expansion of Ag via Au-

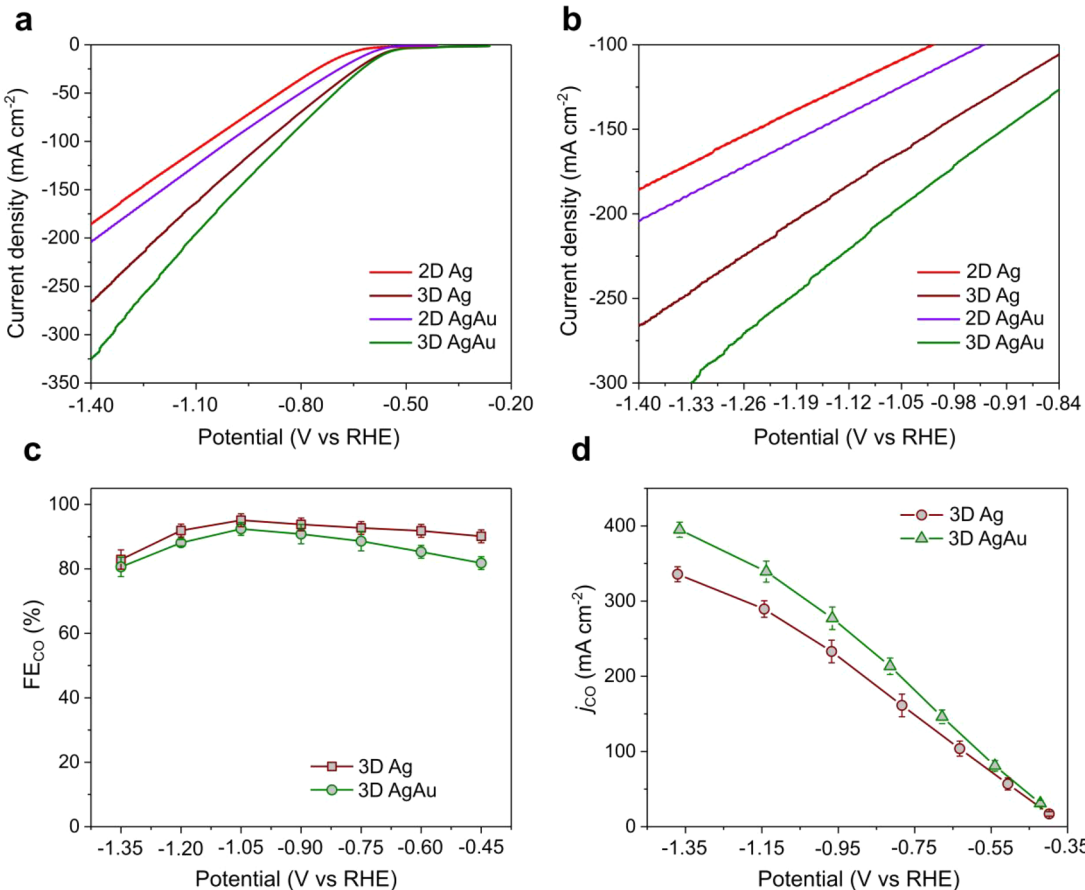


Figure 4. CO_2 -to-CO conversion performance of planar (2D) and high-surface-area (3D) AgAu and Ag control catalysts in a liquid-electrolyte flow cell. (a) Linear sweep voltammetry curves in a potential window of -0.20 and -1.40 V versus RHE. (b) Linear sweep voltammetry curves in a potential window of -0.84 and -1.40 V versus RHE. (c) CO FE versus potential. (d) CO partial current density versus potential. Operating conditions: 1 M KHCO_3 was supplied to the cathodic and anodic flow chambers with a flow rate of 20 mL min^{-1} ; CO_2 was supplied to the cathodic gas chamber with a flow rate of $\sim 50\text{ sccm}$; experiments were performed under room temperature and pressure. The linear sweep voltammetry curves were obtained by sweeping the voltage from -0.2 to -1.4 V versus RHE with a constant scan rate of 25 mV . Each linear sweep voltammetry curve is the representative of 15 scans from three independent measurements. Potentials are presented with iR compensation. The error bars correspond to the standard deviation of three independent measurements. Note: 2D Ag catalyst stands for planar (2D) Ag/PTFE, 2D AgAu catalyst stands for Au-doped planar Ag/PTFE (with an optimized galvanic-replacement duration of 15 min), 3D AgAu catalyst stands for Au-doped Ag NPs supported on planar 2D AgAu catalyst (each with an optimized galvanic-replacement duration of 15 min), and 3D Ag catalyst stands for Ag NPs supported on planar 2D Ag catalyst.

doping (Figure 2c). We detected similar negative shifts and spectra for galvanic-replacement durations ranging from 5 to 30 min , indicating that Au modifies the lattice of Ag prior to forming islands of Au adparticles on the surface. We then carried out *in situ* X-ray absorption spectroscopy (XAS) measurements and confirmed the alloyed AgAu structures via the extended X-ray absorption fine structure (EXAFS) analysis. Through EXAFS fitting, we found a decrease of Au coordination with galvanic-replacement durations in the range of 10 – 15 min , signifying the formation of surface Au adparticles at the AgAu alloy interface under these conditions (Figure 2d,e and see Figures S8–S11 and Table S3 for additional XAS data). With longer replacement durations we observed an increase in the density of Au adparticles (Figure 2d and see Figures S8–S11 and Table S3 for additional XAS data), in agreement with the SEM results (Figure S4).

We assessed the initial CO_2 RR performance of the 2D AgAu catalysts in a flow cell with 1 M KHCO_3 liquid electrolyte (see Figure S12 and Tables S4–S8 for performance data). With galvanic-replacement durations in the range of 0 – 15 min , the peak CO partial current density increases from 160 to 183 mA cm^{-2}

, with a reduction in the corresponding cathodic overpotential from -1.34 to -1.16 V versus RHE (Figure 1a,b and see Tables S4–S6 for additional performance data), Tafel analyses of CO productivities from CO_2 on 2D AgAu exhibit a slope of 82 mV dec^{-1} , lower than that of Ag (137 mV dec^{-1}) (see Figure S4 for Tafel slopes), indicating a faster electron transfer for CO formation. Further extending the duration (from 15 to 30 min) did not improve performance, instead leading to a higher HER activity and a lower peak CO partial current density (see Figure S12 and Tables S6–S8 for additional performance data)—outcomes we attribute to excessive Au surface coverage. Despite the HER activity at low applied potentials ($\sim -0.4\text{ V}$ versus RHE), the 2D AgAu catalyst combines high CO selectivity and low overpotential at reaction rates $> 120\text{ mA cm}^{-2}$ (Figure 1a,b).

To further boost current densities at similar cathodic overpotentials, we sought to extend the reaction interface by translating the Au-doping strategy to a 3D catalyst motif, in which Au-doped Ag nanoparticles (NPs) are supported on 2D AgAu catalysts (see Supporting Information methods for details and see Figure 3 and Figures S13–S16 for the

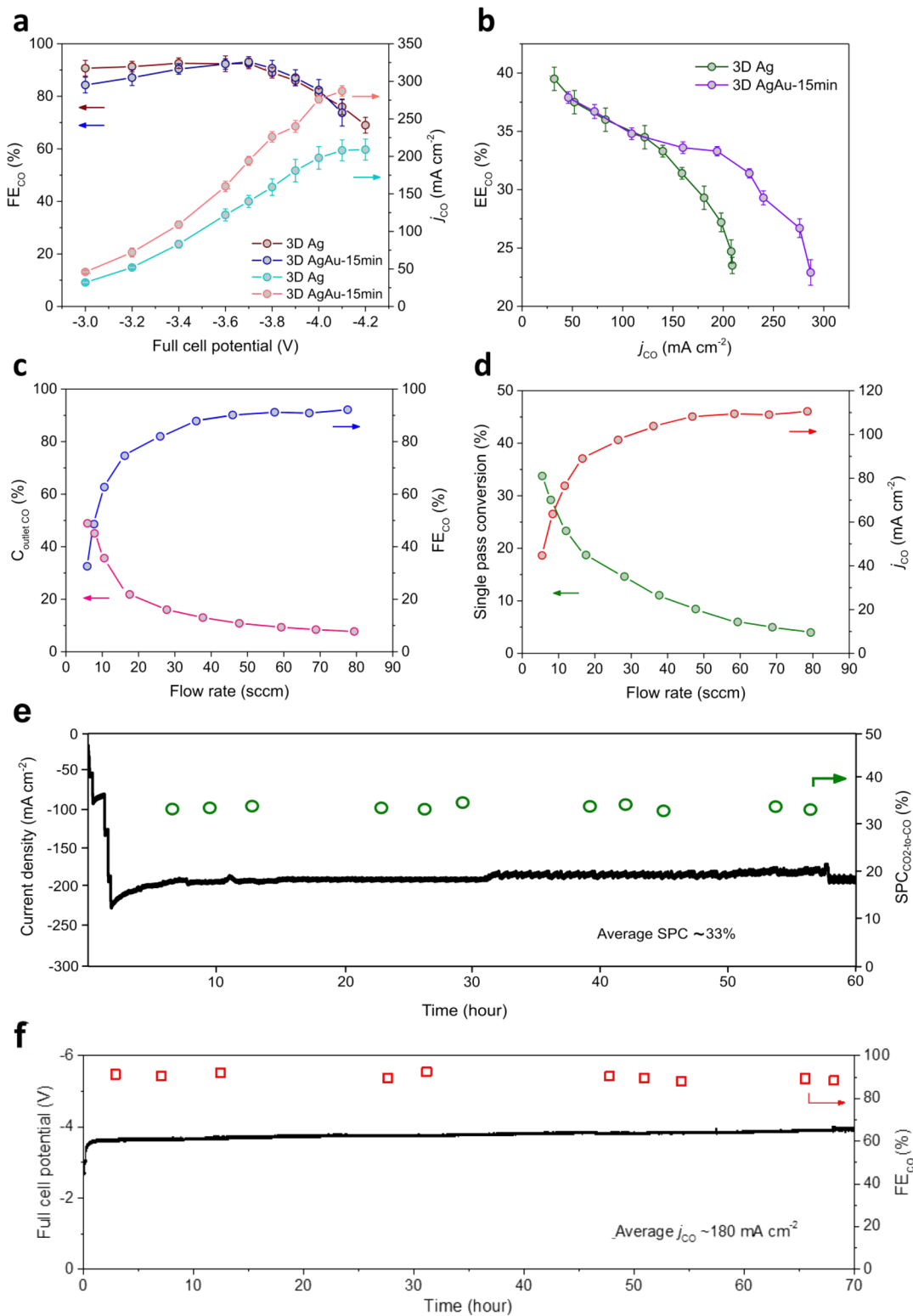


Figure 5. CO_2 -to-CO conversion performance of 3D AgAu and Ag control catalysts in a catholyte-free membrane electrode assembly (MEA) electrolyzer. (a) CO FE and CO partial current density versus full-cell potential for 3D AgAu and Ag control catalysts. (b) CO EE versus CO partial current density for 3D AgAu and Ag control catalysts. (c) CO concentration (molar ratio) at the cathode outlet versus reactant CO_2 flow rate for 3D AgAu catalyst. (d) Single pass conversion of CO_2 toward CO versus flow rate for 3D AgAu catalyst. (e) Extended single pass conversion of CO_2 toward CO at a constant full-cell potential of -3.8 V (an average current density of 185 mA cm^{-2} ; humidified CO_2 with a flow rate of $\sim 15 \text{ sccm}$; 0.1 M KHCO_3 anolyte with a flow rate of 15 mL/min ; ambient pressure and temperature). The black line represents the full-cell potential recorded during the extended CO_2 electrolysis (primary y -axis). Each green circle represents the single pass conversion averaged from three independent samples (secondary y -axis). (f) Extended CO_2 -to-CO conversion performance of 3D AgAu catalyst at a constant current density of 200 mA cm^{-2} (humidified CO_2 with a flow rate of $\sim 80 \text{ sccm}$; 0.1 M KHCO_3 anolyte with a flow rate of 15 mL/min ; ambient pressure and temperature). The black line represents the full-cell potential recorded during the extended CO_2 electrolysis (primary y -axis). Each red square

Figure 5. continued

represents the CO FE averaged from three independent samples (secondary y-axis). Operating conditions for the performance experiments: 0.1 M KHCO₃ used as the anolyte; humidified CO₂ with a flow rate of ~80 sccm (except for single pass conversion measurements) supplied to the cathode; experiments performed under room temperature and pressure. Full-cell potentials are presented without *iR* compensation. The error bars correspond to the standard deviation of three independent measurements. Note: 3D AgAu catalyst stands for Au-doped Ag NPs supported on planar 2D AgAu catalyst and 3D Ag catalyst stands for Ag NPs supported on planar 2D Ag catalyst.

morphology and microstructure of the electrodes). We explored the electrochemical performance of the 3D AgAu catalysts and 3D Ag controls in a liquid-electrolyte flow cell electrolyzer. We find that the working principle of the 3D AgAu catalysts is akin to that of the 2D AgAu catalysts: AgAu catalysts enable greater CO productivities with lower cathodic overpotentials over a wide range of current densities (Figure 4a,b—cyclic voltammetry (CV) curves of the 3D catalyst). The 3D AgAu catalysts enabled a peak CO partial current density of $408 \pm 15 \text{ mA cm}^{-2}$ (at -1.36 V versus RHE), compared to $340 \pm 12 \text{ mA cm}^{-2}$ for the 3D Ag control case (see Tables S9 and S10 for additional experimental data). The extended reaction interface in the 3D AgAu catalyst also promoted CO productivity compared to the 2D AgAu catalyst (Figure 4c,d and see Tables S6 and S9 for experimental data). The 3D AgAu catalyst—in the context of its high CO selectivity and productivity—is among the best low-temperature, neutral-media CO₂-to-CO catalysts in literature.

We then sought to adapt this activity promoting catalyst strategy to a membrane electrode assembly (MEA)—a catholyte-free electrolyzer platform that enables stable CO₂ electrolysis.³⁰ The MEA system enabled us to assess the practicality of our catalyst in a scalable, energy efficient, stable electrolyzer using a neutral electrolyte at the anode. Iridium oxide (IrO₂) on a titanium felt, a commercial anion exchange membrane (AEM), and the 3D AgAu catalysts were used as the anode electrode, electrolyte, and cathode, respectively (see Supporting Information methods for details). Exploring CO₂RR performance at a voltage range of -3 to -4.2 V , we find that CO FE increases with increasing cell potential, reaching a plateau of $93 \pm 1\%$ at a CO partial current density of $186 \pm 3 \text{ mA cm}^{-2}$. The 3D AgAu catalysts delivered CO FEs above 90% up to current densities of $\sim 240 \text{ mA cm}^{-2}$. While the increasing applied potential led to an increase in HER activity, the system delivered a peak CO partial current density of $302 \pm 12 \text{ mA cm}^{-2}$ at a full-cell potential of -4.1 V (Figure 5a and see Table S11 for additional experimental data). In contrast, the MEA system with the 3D Ag control catalysts provided a lower peak CO partial current density of $204 \pm 9 \text{ mA cm}^{-2}$ and required a full-cell potential of -4.2 V (Figure 5a and see Table S12 for additional experimental data). The MEA system with the 3D AgAu catalysts achieved a peak CO full-cell EE of $37 \pm 1\%$ at a CO partial current density of $43 \pm 1 \text{ mA cm}^{-2}$, and the full-cell EE remained above 30% up to a partial current density of $247 \pm 6 \text{ mA cm}^{-2}$ (see Table S11 for additional experimental data). In contrast, the full-cell energy efficiency of the 3D Ag control case dropped below 30% at CO partial current densities greater than $163 \pm 5 \text{ mA cm}^{-2}$ (Figure 5b and see Table S12 for additional experimental data). Performing CV measurements in a full-cell system, we further confirmed a voltage difference of 0.2 – 0.25 V between the 3D AgAu and 3D Ag control catalysts over a wide range of current densities (see Figure S17 for CV curves of 3D AgAu and 3D Ag control).

We further assessed the performance of the 3D AgAu MEA system with respect to single pass conversion, SPC—a critically important performance metric in CO₂RR (Figure 5c,d). We constrained the flow rate while performing CO₂RR at a constant current density of 120 mA cm^{-2} . The CO FE remained above 80% at downstream flow rates from 80 to 30 sccm, although reducing the flow rate further led to a severe loss of CO selectivity (Figure 5c). The 3D AgAu catalyst delivered a cathodic gas stream with a peak 48% CO (molar ratio) and a peak SPC of 34% for CO₂-to-CO conversion (Figure 5c,d). When run at an average current density of 185 mA cm^{-2} , the 3D AgAu catalyst maintains an SPC of 33% during continuous operation (Figure 5e). Although constraining the flow rate of inlet CO₂ to 15 sccm results in a decrease in productivity and energy efficiency, the 3D AgAu catalyst maintains a CO partial current density of $\sim 130 \text{ mA cm}^{-2}$ and a CO energy efficiency of $\sim 25\%$.

The 3D AgAu catalyst was stable, providing an average CO FE of $\sim 90\%$ and average CO full-cell EE of 32% for over 60 h of continuous operation (Figure 5f). We found, by performing SEM, EDX, and XPS, the catalyst maintained its morphology and composition through the extended CO₂-to-CO conversion (see Figures S18 and S19 for the SEM, EDX, and XPS data).

In summary, we present an activity promoting strategy that enables low overpotential and selective CO₂-to-CO conversion at industrially relevant reaction rates and EEs. We achieve this by developing AgAu catalysts synthesized through galvanic replacement between Ag and Au. Benefiting from the low energy barrier for formation of a key reaction intermediate (${}^{\ast}\text{COOH}$), we achieved onset potential reductions of up to $\sim 200 \text{ mV}$ over a wide range of CO partial current densities (100 – 400 mA cm^{-2}). We demonstrated this strategy in both flow cell and MEA electrolyzer formats with neutral-media electrolytes. In an MEA electrolyzer, high-surface-area AgAu catalysts enabled CO FEs of $>90\%$ and CO full-cell EEs of $>30\%$ up to a CO partial current density of $247 \pm 6 \text{ mA cm}^{-2}$. The AgAu catalysts were stable, converting CO₂-to-CO conversion for over 60 h at high reaction rates ($\geq 185 \text{ mA cm}^{-2}$) under both high and low CO₂ reactant availability conditions. The AgAu catalyst—in the context of its high selectivity, productivity, energy efficiency, and stability—is among the best low-temperature, neutral-media CO₂-to-CO catalysts in literature (see Table S13 for comparison).

ASSOCIATED CONTENT

Supporting Information

The Supporting Information is available free of charge at <https://pubs.acs.org/doi/10.1021/acsaem.1c01577>.

Experimental details and additional data (PDF)

AUTHOR INFORMATION

Corresponding Authors

David Sinton — Department of Mechanical and Industrial Engineering, University of Toronto, Toronto, Ontario M5S

3G8, Canada;  orcid.org/0000-0003-2714-6408;
Email: sinton@mie.utoronto.ca

Edward H. Sargent — Department of Electrical and Computer Engineering, University of Toronto, Toronto, Ontario M5S 3G4, Canada;  orcid.org/0000-0003-0396-6495;
Email: ted.sargent@utoronto.ca

Authors

Adnan Ozden — Department of Mechanical and Industrial Engineering, University of Toronto, Toronto, Ontario M5S 3G8, Canada

Yanjiang Liu — Department of Electrical and Computer Engineering, University of Toronto, Toronto, Ontario M5S 3G4, Canada

Cao-Thang Dinh — Department of Electrical and Computer Engineering, University of Toronto, Toronto, Ontario M5S 3G4, Canada; Department of Chemical Engineering, Queen's University, Kingston, Ontario K7L 3N6, Canada;
 orcid.org/0000-0001-9641-9815

Jun Li — Department of Mechanical and Industrial Engineering, University of Toronto, Toronto, Ontario M5S 3G8, Canada; Department of Electrical and Computer Engineering, University of Toronto, Toronto, Ontario M5S 3G4, Canada

Pengfei Ou — Department of Electrical and Computer Engineering, University of Toronto, Toronto, Ontario M5S 3G4, Canada;  orcid.org/0000-0002-3630-0385

F. Pelayo García de Arquer — Department of Electrical and Computer Engineering, University of Toronto, Toronto, Ontario M5S 3G4, Canada;  orcid.org/0000-0003-2422-6234

Complete contact information is available at:

<https://pubs.acs.org/10.1021/acsaem.1c01577>

Author Contributions

D.S. and E.H.S. supervised the project. A.O. and C.-T.D. conceived the idea. A.O. and C.-T.D. synthesized the AgAu catalysts and carried out all of the electrochemical experiments. A.O. carried out SEM, TEM, XPS, and XRD measurements. J.L. performed the XAS measurements. Y.L. and P.O. performed the DFT calculations and wrote the corresponding sections. A.O. wrote the manuscript. F.P.G.d.A. contributed to data analysis. All authors discussed the results and assisted during manuscript preparation.

Author Contributions

¶A.O., Y.L., and C.-T.D. contributed equally to this work.

Notes

The authors declare no competing financial interest.

ACKNOWLEDGMENTS

We acknowledge financial support from the Ontario Research Fund: Research Excellence Program, the Natural Sciences and Engineering Research Council (NSERC) of Canada. X-ray absorption spectra were performed on SXRMb beamlines at the Canadian Light Source (CLS), which is supported by the Canada Foundation for Innovation, Natural Sciences and Engineering Research Council of Canada, the University of Saskatchewan, the Government of Saskatchewan, Western Economic Diversification Canada, the National Research Council Canada, and the Canadian Institutes of Health Research. We acknowledge the Ontario Centre for the Characterization of Advanced Materials (OCCAM) for sample

preparation and characterization facilities. J.L. acknowledges the Banting postdoctoral fellowship. D.S. acknowledges the NSERC E.W.R. Steacie Memorial Fellowship.

REFERENCES

- (1) Garcia de Arquer, F. P.; Dinh, C.-T.; Ozden, A.; Wicks, J.; McCallum, C.; Kirmani, A. R.; Nam, D.-H.; Gabardo, C.; Seifitokaldani, A.; Wang, X.; Li, Y. C.; Li, F.; Edwards, J.; Richter, L. J.; Thorpe, S. T.; Sinton, D.; Sargent, E. H. CO₂ electrolysis to multicarbon products at activities greater than 1 A cm⁻². *Science* **2020**, *367*, 661–667.
- (2) Wang, Y.; Wang, Z.; Dinh, C.-T.; Li, J.; Ozden, A.; Golam Kibria, M.; Seifitokaldani, A.; Tan, C.-S.; Gabardo, C. M.; Luo, M.; Zhou, H.; Li, F.; Lum, Y.; McCallum, C.; Xu, Y.; Liu, M.; Proppe, A.; Johnston, A.; Todorovic, P.; Zhuang, T.-T.; Sinton, D.; Kelley, S. O.; Sargent, E. H. Catalyst synthesis under CO₂ electroreduction favours faceting and promotes renewable fuels electrosynthesis. *Nat. Catal.* **2020**, *3*, 98–106.
- (3) Ozden, A.; Li, F.; Garcia de Arquer, F. P.; Rosas-Hernandez, A.; Thevenon, A.; Wang, Y.; Hung, S.-F.; Wang, X.; Chen, B.; Li, J.; Wicks, J.; Luo, M.; Wang, Z.; Agapie, T.; Peters, J. C.; Sargent, E. H.; Sinton, D. High-rate and efficient ethylene electrosynthesis using a catalyst/promoter/transport layer. *ACS Energy Lett.* **2020**, *5*, 2811–2818.
- (4) Ozden, A.; Wang, Y.; Li, F.; Luo, M.; Sisler, J.; Thevenon, A.; Rosas-Hernandez, A.; Burdyny, T.; Lum, Y.; Yadegari, H.; Agapie, T.; Peters, J. C.; Sargent, E. H.; Sinton, D. Cascade CO₂ electroreduction enables efficient carbonate-free production of ethylene. *Joule* **2021**, *5*, 706–719.
- (5) Li, J.; Wang, Z.; McCallum, C.; Xu, Y.; Li, F.; Wang, Y.; Gabardo, C. M.; Dinh, C.-T.; Zhuang, T.-T.; Wang, L.; Howe, J. Y.; Ren, Y.; Sargent, E. H.; Sinton, D. Constraining CO coverage on copper promotes high-efficiency ethylene production. *Nat. Catal.* **2019**, *2*, 1124–1131.
- (6) Raciti, D.; Wang, C. Electrochemical alternative to Fischer-Tropsch. *Nat. Catal.* **2018**, *1*, 741–742.
- (7) Luc, W.; Fu, X.; Shi, J.; Lv, J.-J.; Jouny, M.; Ko, B. H.; Xu, Y.; Tu, Q.; Hu, X.; Wu, J.; Yue, Q.; Liu, Y.; Jiao, F.; Kang, Y. Two-dimensional copper nanosheets for electrochemical reduction of carbon monoxide to acetate. *Nat. Catal.* **2019**, *2*, 423–430.
- (8) Ripatti, D. S.; Veltman, T. R.; Kanan, M. W. Carbon monoxide gas diffusion electrolysis that produces concentrated C₂ products with high single-pass conversion. *Joule* **2019**, *3*, 240–256.
- (9) Li, J.; Xu, A.; Li, F.; Wang, Z.; Zou, C.; Gabardo, C. M.; Wang, Y.; Ozden, A.; Xu, Y.; Nam, D.-H.; Lum, Y.; Wicks, J.; Chen, B.; Wang, Z.; Chen, J.; Wen, Y.; Zhuang, T. T.; Luo, M.; Du, X.; Sham, T.-K.; Zhang, B.; Sargent, E. H.; Sinton, D. Enhanced multi-carbon alcohol electroproduction from CO via modulated hydrogen adsorption. *Nat. Commun.* **2020**, *11*, 3685.
- (10) Wang, X.; Wang, Z.; Zhuang, T.-T.; Dinh, C.-T.; Li, J.; Nam, D.-H.; Li, F.; Huang, C.-W.; Tan, C.-H.; Chen, Z.; Chi, M.; Gabardo, C. M.; Seifitokaldani, A.; Todorovic, P.; Proppe, A.; Pang, Y.; Kirmani, A. R.; Wang, Y.; Ip, A. H.; Richter, L. J.; Scheffel, B.; Xu, A.; Lo, S.-C.; Kelley, S. O.; Sinton, D.; Sargent, E. H. Efficient upgrading of CO to C₃ fuel using asymmetric C-C coupling active sites. *Nat. Commun.* **2019**, *10*, 5186.
- (11) Dinh, C.-T.; Garcia de Arquer, F. P.; Sinton, D.; Sargent, E. H. High Rate, selective, and stable electroreduction of CO₂ to CO in basic and neutral media. *ACS Energy Lett.* **2018**, *3*, 2835–2840.
- (12) Kutz, R. B.; Chen, Q.; Yang, H.; Sajjad, S. D.; Liu, Z.; Masel, I. R. Sustainion Imidazolium-Functionalized Polymers for Carbon Dioxide Electrolysis. *Energy Technol. (Weinheim, Ger.)* **2017**, *5*, 929–936.
- (13) Jiang, K.; Siahrostami, S.; Akey, A. J.; Li, Y.; Lu, Z.; Lattimer, J.; Hu, Y.; Stokes, C.; Gangishetty, M.; Chen, G.; Zhou, Y.; Hill, W.; Cai, W.-B.; Bell, D.; Chan, K.; Nørskov, J. K.; Cui, Y.; Wang, H. Transition-Metal Single Atoms in a Graphene Shell as Active Centers for Highly Efficient Artificial Photosynthesis. *Chem* **2017**, *3*, 950–960.

- (14) Kortlever, R.; Shen, J.; Schouten, K. J. P.; Calle-Vallejo, F.; Koper, M. T. M. Catalysts and Reaction Pathways for the Electrochemical Reduction of Carbon Dioxide. *J. Phys. Chem. Lett.* **2015**, *6*, 4073–4082.
- (15) Zheng, T.; Jiang, K.; Wang, H. Recent Advances in Electrochemical CO₂-to-CO Conversion on Heterogeneous Catalysts. *Adv. Mater.* **2018**, *30*, 1802066.
- (16) Rosen, B. A.; Salehi-Khojin, A.; Thorson, M. R.; Zhu, W.; Whipple, D. T.; Kenis, P. J. A.; Masel, R. I. Ionic Liquid-Mediated Selective Conversion of CO₂ to CO at Low Overpotentials. *Science* **2011**, *334*, 643–644.
- (17) Ma, M.; Trzesniewski, B. J.; Xie, J.; Smith, W. A. Selective and Efficient Reduction of Carbon Dioxide to Carbon Monoxide on Oxide-Derived Nanostructured Silver Electrocatalysts. *Angew. Chem., Int. Ed.* **2016**, *55*, 9748–9752.
- (18) Lu, Q.; Rosen, J.; Zhou, Y.; Hutchings, G. S.; Kimmel, Y. C.; Chen, J. G.; Jiao, F. A selective and efficient electrocatalyst for carbon dioxide reduction. *Nat. Commun.* **2014**, *5*, 3242.
- (19) Mariano, R. G.; Kang, M.; Wahab, O. J.; McPherson, I. J.; Rabinowitz, J. A.; Unwin, P. R.; Kanan, M. W. Microstructural origin of locally enhanced CO₂ electroreduction activity on gold. *Nat. Mater.* **2021**, *20*, 1000–1006.
- (20) Liu, M.; Pang, Y.; Zhang, B.; De Luna, P.; Voznyy, O.; Xu, J.; Zheng, X.; Dinh, C.-T.; Fan, F.; Cao, C.; de Arquer, F. P. G.; Safaei, S.; Mepham, A.; Klinkova, A.; Kumacheva, E.; Filletter, T.; Sinton, D.; Kelley, S. O.; Sargent, E. H. Enhanced electrocatalytic CO₂ reduction via field-induced reagent concentration. *Nature* **2016**, *537*, 382–386.
- (21) Xia, R.; Zhang, S.; Ma, X.; Jiao, F. Surface-functionalized palladium catalysts for electrochemical CO₂ reduction. *J. Mater. Chem. A* **2020**, *8*, 15884–15890.
- (22) Gao, D.; Zhou, H.; Wang, J.; Miao, S.; Yang, F.; Wang, G.; Wang, J.; Bao, X. Size-Dependent Electrocatalytic Reduction of CO₂ over Pd Nanoparticles. *J. Am. Chem. Soc.* **2015**, *137*, 4288–4291.
- (23) DiMeglio, J. L.; Rosenthal, J. Selective Conversion of CO₂ to CO with High Efficiency Using an Inexpensive Bismuth-Based Electrocatalyst. *J. Am. Chem. Soc.* **2013**, *135*, 8798–8801.
- (24) Kim, C.; Jeon, H. S.; Eom, T.; Jee, M. S.; Kim, H.; Friend, C. M.; Min, B. K.; Hwang, Y. J. Achieving Selective and Efficient Electrocatalytic Activity for CO₂ Reduction Using Immobilized Silver Nanoparticles. *J. Am. Chem. Soc.* **2015**, *137*, 13844–13850.
- (25) Gu, J.; Hsu, C.-S.; Bai, L.; Chen, H. M.; Hu, X. Atomically dispersed Fe₃₊ sites catalyze efficient CO₂ electroreduction to CO. *Science* **2019**, *364*, 1091–1094.
- (26) Verma, S.; Hamasaki, Y.; Kim, C.; Huang, W.; Lu, S.; Jhong, H.-R.J.; Gewirth, A. A.; Fujigaya, T.; Nakashima, N.; Kenis, P. J. A. Insights into the Low Overpotential Electroreduction of CO₂ to CO on a Supported Gold Catalyst in an Alkaline Flow Electrolyzer. *ACS Energy Lett.* **2018**, *3*, 193–198.
- (27) Ren, S.; Joulie, D.; Salvatore, D.; Torbensen, K.; Wang, M.; Robert, M.; Berlinguette, C. Molecular electrocatalysts can mediate fast, selective CO₂ reduction in a flow cell. *Science* **2019**, *365*, 367–369.
- (28) Peterson, A. A.; Norskov, J. K. Activity descriptors for CO₂ electroreduction to methane on transition-metal catalysts. *J. Phys. Chem. Lett.* **2012**, *3*, 251–258.
- (29) Back, S.; Kim, J.-H.; Kim, T.-T.; Jung, Y. Bifunctional interface of Au and Cu for improved CO₂ electroreduction. *ACS Appl. Mater. Interfaces* **2016**, *8*, 23022–23027.
- (30) Li, F.; Thevenon, A.; Rosas-Hernandez, A.; Wang, Z.; Li, Y.; Gabardo, C. M.; Ozden, A.; Dinh, C.-T.; Li, J.; Wang, Y.; Edwards, J. P.; Xu, Y.; McCallum, C.; Tao, L.; Liang, Z.-Q.; Luo, M.; Wang, X.; Li, H.; O'Brien, C. P.; Tan, C.-H.; Nam, D.-H.; Quintero-Bermudez, R.; Zhuang, T.-T.; Li, Y. C.; Han, Z.; Britt, R. D.; Sinton, D.; Agapie, T.; Peters, J. C.; Sargent, E. H. Molecular tuning of CO₂-to-ethylene conversion. *Nature* **2020**, *577*, 509–513.